Depolarized Scattering of Rough Surface With Dielectric Inhomogeneity and Spatial Anisotropy

Ying Yang, *Member, IEEE*, Kun-Shan Chen, *Fellow, IEEE*, Xiaofeng Yang, *Senior Member, IEEE*, Zhao-Liang Li, *Senior Member, IEEE*, and Jiangyuan Zeng, *Member, IEEE*

***Abstract*— This article presents a new index, polarization-conversion ratio (PCR) to characterize depolarized bistatic scattering from rough surfaces with dielectric inhomogeneity and spatial anisotropy. We then investigate the dependence of PCR on both surface and radar parameters. Numerical results show that the distribution of PCR on the scattering plane varies with the polarization state of the incident wave and incident angle. The PCR clusters more in the cross-plane for horizontally polarized incidence. However, for vertically polarized incidence, the PCR disperses as "triangular shape" on the whole scattering plane with a sharp valley occurring in the incident plane. The following points can be drawn: 1) the inhomogeneity effectively enhances the PCR in the cross-plane; 2) the effect of anisotropy on the PCR is relatively weak, because the scattering is less affected by correlation length; 3) the impacts of surface rms height on the PCR are negative on the whole scattering plane; and 4) as the background permittivity increases, at the horizontally polarized incidence, the PCR is enhanced in the backward and forward regions, while at vertically polarized incidence, it is enhanced in the incident plane and the forward region. As is demonstrated, the PCR is an effective measure of the sensitivity of depolarization, making it potentially useful as a new reliable index for surface parameter inversion.**

***Index Terms*— Anisotropy, bistatic scattering, depolarization, inhomogeneous, polarization conversion, rough surface.**

I. Introduction

POLARIZATION, as one of the inherent properties of electromagnetic (EM) waves, is of practical significance to many applications [1]–[4]. Artificial devices have been developed to control and manipulate the polarization of the EM waves, such as invisibility cloaks, antenna system, polarization beam splitters, and perfect absorbers [5]–[7]. Given its inherent properties, polarization conversion has been proposed in the microwave [8], [9], terahertz [10], infrared [11], and visible [12] frequency fields for metasurfaces. By different structures of the metamaterial, the linear polarization of the incident waves can be converted into the orthogonal direction, and the right-hand circularly polarized incident waves can also be converted into the left-hand circularly polarized wave [13]–[15]. When the EM waves travel through the metamaterial, the polarization conversion for both the linearly and circularly polarized waves can be observed. In remote sensing applications, exploring EM scattering for the natural surface's 3-D structures is of increasing importance.

The spatial anisotropy of the rough soil surface may be formed either by natural force (e.g., dune) or by plowing or raking practice in the agricultural field. The permittivity distribution is nonuniform in depth [16], due to, for example, the evapotranspiration process of the soil moisture content [17]. In some real physical scenarios, the wind-induced dunes and the ridged land surface by plowing are azimuthally anisotropic. From the experimental measurements reported in [18], the relative complex dielectric constant curves as a function of volumetric soil moisture content. In remote sensing applications, the soil moisture profile is of particular interest for its prominent role in the climatic and hydrologic modelings [19]–[21]. Extensive studies of wave-scattering inhomogeneous rough surfaces have been conducted in the past decades. The reflection coefficient from the vertically inhomogeneous media whose permittivity is a function of depth was reported [22]. Sarabandi and Chiu [23] derived the bistatic scattering coefficients of the soil surface with a slight rough interface and inhomogeneous dielectric profile. A similar study was also carried out by a small perturbation method (SPM) for a slightly rough boundary [24]. Tsang *et al*. [25] developed the EM full-wave simulations for the volume scattering of dense media with terrestrial snow. Komarov *et al.* [26] analyzed the EM wave scattering from rough boundaries interfacing inhomogeneous media and applied the formulation to study snow-covered sea ice. Zamani *et al*. [27] reported a perturbation approach, the extended boundary condition (EBC)-based SPM to study the scattering from inhomogeneous media with arbitrary dielectric profiles. A translation matrix (T-Matrix) solution to the 3-D EM scattering from the dielectric layered medium was proposed in [28].

Manuscript received April 18, 2020; revised May 30, 2020; accepted May 30, 2020. Date of publication June 11, 2020; date of current version December 24, 2020. This work was supported in part by the China Postdoctoral Research Science Foundation under Grant 2019M663414, in part by Initiative Funding of Guilin University of Technology under Grant GUTQDJJ2019146, in part by the National Natural Science Foundation of China under Grant 41871268Y, and in part by the National Natural Science Foundation of China under Grant 41971317. *(Corresponding author: Kun-Shan Chen.)*

Ying Yang and Kun-Shan Chen are with the College of Geomantic and Geoinformation, Guilin University of Technology, Guilin 541004, China (e-mail: yangying@glut.edu.cn; chenks@radi.ac.cn).

Xiaofeng Yang and Jiangyuan Zeng are with the State Key Laboratory of Remote Sensing Science, Institute of Remote Sensing and Digital Earth, Chinese Academy of Sciences, Beijing 100101, China, and also with Beijing Normal University, Beijing 100101, China (e-mail: yangxf@radi.ac.cn; zengjy@radi.ac.cn).

Zhao-Liang Li is with the Institute of Agricultural Resources and Regional Planning, Chinese Academy of Agricultural Sciences, Beijing 100081, China (e-mail: lizl@unistra.fr).

Color versions of one or more of the figures in this article are available online at https://ieeexplore.ieee.org.

Digital Object Identifier 10.1109/TGRS.2020.2999543

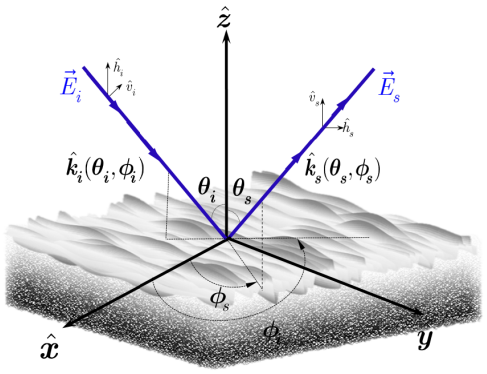

Fig. 1. Scattering geometry of a rough surface.

In the context of spatial anisotropy, Bateson and Woodhouse [29] showed azimuthal backscatter response from the wind-induced sand ripples from scatterometer observation. Bartalis *et al.* [30] demonstrated the azimuthal anisotropy of the scatterometer measurements by the European Remote Sensing Satellite and SeaWinds overland with plowing in the north–south direction. Another example is that Xu *et al.* [31] conducted a full-wave simulation of bistatic scattering from the wind-sculpted sastrugi surface, which resembles a ridge and corrugated structure and can be modeled as a spatially anisotropic surface. More recently, an efficient hybrid method combining the finite-element boundary-integral method with a fast multipole method (FE-BI-FMM) was proposed to study the EM scattering characteristics from a coated object above a two-layered dielectric rough surface at both vertical and horizontal incidences [32]. In addition, the monostatic and bistatic models of the anisotropic rough soil were recently proposed in [33].

It is seen that natural surfaces in many specific physical scenes have both azimuthal anisotropy and dielectric inhomogeneity. Exploring bistatic scattering characteristics and polarization conversion for such surfaces is of practical interest in parameter retrieval. However, from the preceding review of previous works, either dielectric inhomogeneity or spatial anisotropy was considered, but not taking account of both of them simultaneously. Hence, it is the main objective of this article to explore the bistatic scattering characteristics and polarization conversion for rough surfaces with both azimuthal anisotropy and dielectric inhomogeneity. In particular, polarization-conversion ratio (PCR), developed for artificial devices, is applied to characterize the depolarized scattering. This article also attempts to investigate the dependence of PCR on the radar parameters and surface parameters. An advanced integral equation model (AIEM) [34]–[37] is adopted as a working model to simulate the bistatic scattering coefficients.

II. Rough Surface With Dielectric Inhomogeneity and Spatial Anisotropy

Fig. 1 shows the geometry of scattering from a spatially anisotropic rough surface with an inhomogeneous dielectric profile in depth. In Fig. 1, $\hat{k}_s(\theta_s,\phi_s)$ and $\hat{k}_i(\theta_i,\phi_i)$ denote the scattering- and incident-wave unit vectors, respectively, θ_i and ϕ_i are the incident angle and the incident azimuthal angle, and θ_s and ϕ_s are the scattering angle and the scattering azimuthal angle. In backscattering, $\theta_s = \theta_i$ and $\phi_s = \phi_i + 180°$. The spatial anisotropy can be statistically described by a directional correlation function $\rho(r,\psi)$, where r is the lag distance and ψ is the direction from 0° to 360°, and the inhomogeneity is modeled by dielectric profiles $\varepsilon_r(z)$.

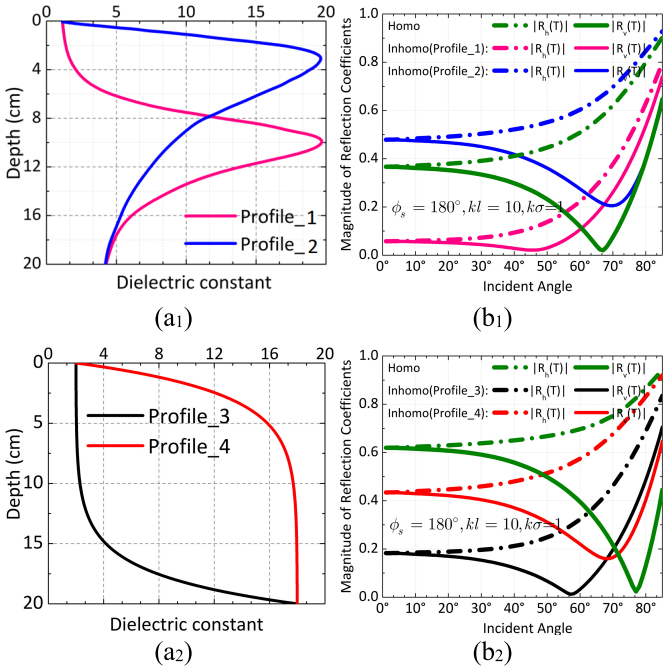

Fig. 2. (a_1) Profiles_1 and 2 with the same maximum dielectric constant of $20 - j2.0$ and background dielectric constant of $4.5 - j0.45$. (a_2) Profiles_3 and 4 with the same background dielectric constant of $18 - j1.8$ at $f = 1.25$ GHz. Comparison in magnitude of reflection coefficients between the homogeneous and inhomogeneous surfaces with (b_1) profiles_1 and 2 and (b_2) profiles_3 and 4.

A. Inhomogeneity

For an inhomogeneous rough surface, the permittivity may be vertically nonuniform as a function of depth. For illustration, four typical dielectric profiles with the permittivity varying in the z-direction are chosen [17], [22], [38], [39]. Fig. 2(a1) presents two nonmonotonic dielectric profiles in depth with the same background permittivity of $4.5 - j0.45$ at 1.25 GHz [17]. Indeed, these two dielectric profiles are very common in the soil surface, when the moisture content wets down first and then dries up. The maxima soil moisture of these two dielectric profiles locates at different depths. In addition, the ice-covered surface with fresh or continental ice and clouds with drops of different types and sizes may be modeled by these dielectric profiles. Fig. 2(a2) shows two monotonic dielectric profiles with the same background permittivity of $18 - j0.18$ at 1.25 GHz but with different variation paths [17]. These two profiles can better describe the bare soil after different sunshine times and the sea surface covered with marine ice or fresh ice. Fig. 2(b1) and (b2) demonstrates the reflection coefficients [40], [41] at the horizontally and vertically polarized incidences for these four typical inhomogeneous dielectric profiles. As a reference,

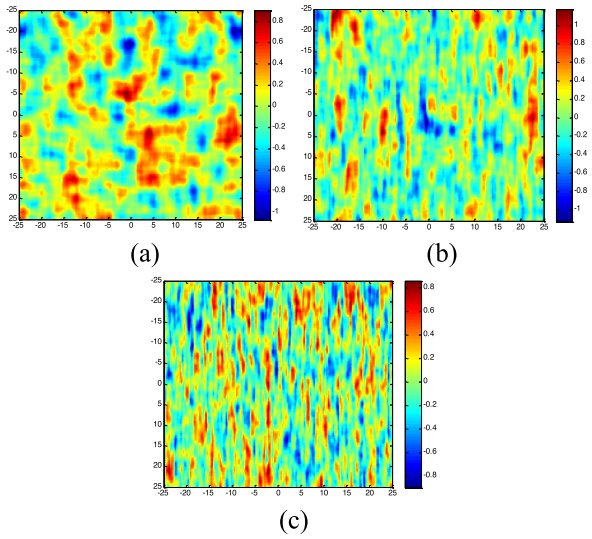

Fig. 3. Numerically generated realization of the rough surfaces with three degrees of anisotropy. (a) Weak anisotropy. (b) Moderate anisotropy. (c) Strong anisotropy.

the reflection coefficients for a homogeneous medium with the same background dielectric constant of the inhomogeneous medium are also given here. It is found that the angular dependence of the reflection coefficients, modeled by the four sets of dielectric profiles, is essentially different, for example, the location of the Brewster angle at vertical polarization. It can be seen that the difference in the reflection coefficients is significant, although the background dielectric constants are the same. The reflection coefficient depends not only on the background dielectric constant but also on the shape and change rate of the dielectric profiles. By comparison with the homogeneous cases, the reflection coefficients of profile_1, profile_3, and profile_4 are relatively small and that of profile_ 2 is high. Both the bistatic scattering characteristics and the PCR for an inhomogeneous medium with different dielectric profiles are examined in a later section.

B. Spatial Anisotropy

Azimuthal anisotropy may be formed by either natural forces or human activities, or even both; for the later, one example is that the ridges on which small roughness rides are created by plowing or raking practice. For EM scattering modeling, the spatial anisotropy can be statistically described by the directional correlation function [42], [43]. The degree of anisotropy can be described by the correlation length varying with azimuthal angle ψ, which is $L(\psi) = L_x \cos^2\psi + L_y \sin^2\psi$ with L_x and L_y being the correlation lengths along two orthogonal directions, and their difference determines the degree of spatial anisotropy. The equivalent correlation length of an anisotropic rough surface is defined by averaging out the directional dependence as $L_e = 1/2\pi \int_0^{2\pi} L(\psi) d\psi$. Fig. 3 illustrates the numerically generated realization for three types of rough surfaces with the degree of anisotropy varying from weak and moderate, to strong. By comparison, the strongly anisotropic rough surface shows greater orientation dependence.

III. Formulations and Polarization-Conversion Ratio

A. Scattering Model

In this article, the scattering coefficient is simulated by an analytical model, the advanced integral equation method (AIEM) [34], [35], which was developed based on the integral equation method (IEM) [2], [35]. The multiple scattering is also included, since it has a significant contribution when the roughness and incident angle are relatively large. For easy reference, here, we summarize the major expressions below. The complete and detailed formulas can be found in [36] and [37]. The scattering coefficient consists of single and multiple scattering terms

$$\sigma_{qp}^{o} = \sigma_{qp}(s) + \sigma_{qp}(m). \tag{1}$$

The single scattering term in (1) remains the same as in [30] and reads as follows:

$$\sigma_{qp}(s) = \frac{k^2}{2} e^{-\sigma^2\left(k_{sz}^2 + k_z^2\right)} \sum_{n=1}^{\infty} \frac{\sigma^{2n}}{n!} \left|\mathrm{I}_{qp}^{n}\right|^2 \mathbf{W}^{(n)}\left(k_{sx} - k_x, k_{sy} - k_y\right) \tag{2}$$

where $k_{sx} = k\sin\theta_s\cos\phi_s$, $k_{sy} = k\sin\theta_s\sin\phi_s$, and $k_{sz} = k\cos\theta_s$ and $k_x = k\sin\theta_i\cos\phi_i$, $k_y = k\sin\theta_i\sin\phi_i$, and $k_z = -k\cos\theta_i$.

The multiple scattering in (1) up to second order, including cross and complementary terms, can be expressed as follows:

$$\sigma_{qp}(m) = \sum_{l=1}^{3} \sigma_{qp}^{kc_l}(m) + \sum_{i=1}^{8} \sigma_{qp}^{c_i}(m) + \sum_{j=9}^{14} \sigma_{qp}^{c_j}(m). \tag{3}$$

The cross term in (3) is an interaction of the Kirchhoff field and the complementary field, which takes the form

$$\begin{aligned}\sigma_{qp}^{kc_l}(m) = \frac{k^2}{8\pi} \mathscr{R}e\Big[f_{qp}^{*} \iint \Big\{ & \mathscr{F}_{qp}^{+}(u,v) g^{kc_l}(u,v,q_1) \\ & + \mathscr{F}_{qp}^{-}(u,v) g^{kc_l}(u,v,-q_1) \\ & \mathscr{G}_{qp}^{+}(u,v) g^{kc_l}(u,v,q_2) \\ & + \mathscr{G}_{qp}^{-}(u,v) g^{kc_l}(u,v,-q_2) \Big\} du dv \Big].\end{aligned} \tag{4}$$

The second and third terms in (3) are the complementary terms. The relevant factors and coefficients appearing in (2)–(4) are referred to [36] and [37].

The scattering coefficients of circular polarizations can be readily given in terms of those of linear polarization [44]

$$\begin{aligned}\sigma_{\mathrm{RR}}^{0} = \frac{1}{4}\Big\{ & \sigma_{\mathrm{vv}}^{0} + \sigma_{\mathrm{hh}}^{0} + \sigma_{\mathrm{vh}}^{0} + \sigma_{\mathrm{hv}}^{0} \\ & - 2\Big[\mathscr{R}e\left(\sigma_{\mathrm{vvhh}}^{0} - \sigma_{\mathrm{vhhv}}^{0}\right) \\ & - \mathscr{I}\left(\sigma_{\mathrm{vvvh}}^{0} + \sigma_{\mathrm{vvhv}}^{0} + \sigma_{\mathrm{vhhh}}^{0} + \sigma_{\mathrm{hvhh}}^{0}\right)\Big]\Big\}\end{aligned} \tag{5}$$

$$\begin{aligned}\sigma_{\mathrm{LR}}^{0} = \frac{1}{4}\Big\{ & \sigma_{\mathrm{vv}}^{0} + \sigma_{\mathrm{hh}}^{0} + \sigma_{\mathrm{vh}}^{0} + \sigma_{\mathrm{hv}}^{0} \\ & + 2\Big[\mathscr{R}e\left(\sigma_{\mathrm{vvhh}}^{0} - \sigma_{\mathrm{vhhv}}^{0}\right) \\ & + \mathscr{I}\left(\sigma_{\mathrm{vvvh}}^{0} - \sigma_{\mathrm{vvhv}}^{0} - \sigma_{\mathrm{vhhh}}^{0} + \sigma_{\mathrm{hvhh}}^{0}\right)\Big]\Big\}\end{aligned} \tag{6}$$

$$\begin{aligned}\sigma_{\mathrm{RL}}^{0} = \frac{1}{4}\Big\{ & \sigma_{\mathrm{vv}}^{0} + \sigma_{\mathrm{hh}}^{0} + \sigma_{\mathrm{vh}}^{0} + \sigma_{\mathrm{hv}}^{0} \\ & + 2\Big[\mathscr{R}e\left(\sigma_{\mathrm{vvhh}}^{0} - \sigma_{\mathrm{vhhv}}^{0}\right) \\ & - \mathscr{I}\left(\sigma_{\mathrm{vvvh}}^{0} - \sigma_{\mathrm{vvhv}}^{0} - \sigma_{\mathrm{vhhh}}^{0} + \sigma_{\mathrm{hvhh}}^{0}\right)\Big]\Big\}\end{aligned} \tag{7}$$

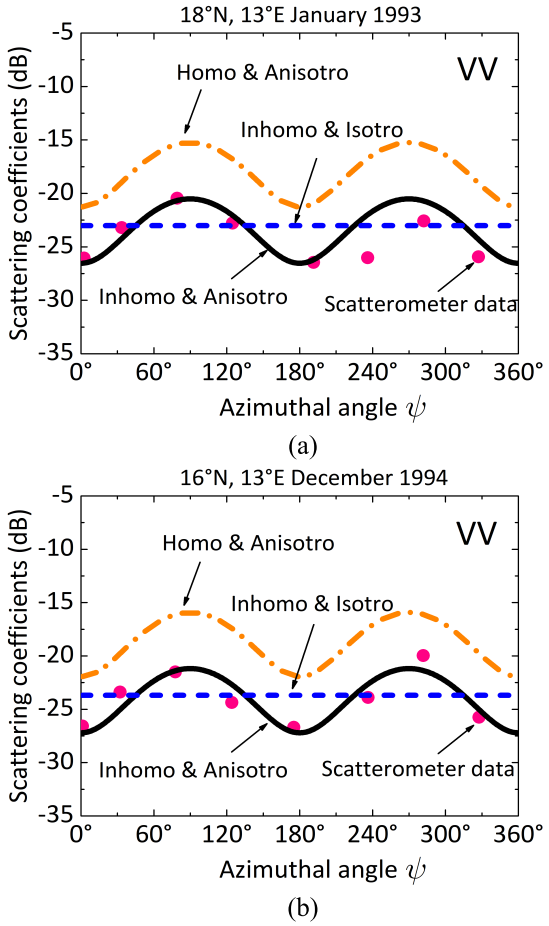

Fig. 4. Comparison of the backscatter azimuthal variations over the dunes region between the model predictions and the scatterometer data [29] acquired by the ERS-1 satellite in (a) 18°N, 13°E, January 1993, $\sigma = 5.2$ cm and (b) 16°N, 13°E, December 1994, $\sigma = 5.4$ cm. Radar parameters: $f = 5.3$ GHz, $\theta_i = 45°$. Surface parameters: $L_x = 10$ cm, $L_y = 20$ cm, $\varepsilon_{rb} = 18 - j1.8$(profile 4).

$$\sigma^0_{\mathrm{LL}} = \frac{1}{4}\{\sigma^0_{\mathrm{vv}} + \sigma^0_{\mathrm{hh}} + \sigma^0_{\mathrm{vh}} + \sigma^0_{\mathrm{hv}} - 2\big[\mathscr{R}e\big(\sigma^0_{\mathrm{vvhh}} - \sigma^0_{\mathrm{vhhv}}\big) + \mathscr{I}\big(\sigma^0_{\mathrm{vvvh}} + \sigma^0_{\mathrm{vvhv}} + \sigma^0_{\mathrm{vhhh}} + \sigma^0_{\mathrm{hvhh}}\big)\big]\}. \quad (8)$$

It is realized that all the last terms in (5)–(8) are relatively small, such that the LL-polarized scattering coefficient is very close to the RR-polarized. Similarly, the LR and RL polarizations are close to each other. Hence, only RR for the like-polarized scattering and the LR for the cross-polarized scattering are discussed in this article. Given the equations displayed in (1)–(8), both linearly or circularly polarized scattering coefficients are the functions of the surface parameters (e.g., correlation length, rms height, dielectric constant, and spectrum) and radar attributes (e.g., incident angle, incident azimuthal angle, scattering angle, scattering azimuthal angle, and frequency). As we mentioned in the previous section, for the anisotropic inhomogeneous rough surface, the permittivity is a function of depth and the correlation length varies as the view azimuthal angle. By applying the new correlation length and the dielectric constant with variables to the AIEM model, the full-polarization scattering coefficient can be calculated.

Before we proceed, let us compare the model predictions and the C-band VV polarization scatterometer data acquired by the ERS-1 satellite between January 1993 (18°N, 13°E) and December 1994 (16°N, 13°E) in the dunes area. The measurement data [29] were collected from the active sand in the north east of Niger, and each pixel is 50 km × 50 km to within a 500-km-wide swath. In this area, the dunes and ripples were formed by the winds. Meanwhile, the sunlight enhanced strength during the day, and the moisture content of the sandy land was nonuniform in the vertical direction. It turned out that such a rough surface could be best described as azimuthal anisotropy and dielectric inhomogeneity. Fig. 4 displays the comparisons between the model predictions and the measurement data. Comparing with the radar scattering for anisotropic homogeneous and anisotropic inhomogeneity alone, the model predictions with anisotropic and inhomogeneous properties are in good agreement with the measurement data for both angular level and trend. The close tracking of peaks and valleys in the azimuthal variation of scattering is observed. The results demonstrate that the AIEM model can be practically useful to model the scattering from the anisotropic inhomogeneous rough surface. Note that in Fig. 15(a), the ascending pass ($0° < \psi < 180°$) measurements are entirely higher than the descending passes ($180° < \psi < 360°$). As reported in [29], a possible explanation for this phenomenon is that the ascending passes are made in the evening and the descending passes in the morning. Ripples produced at the late afternoon winds were larger than those generated by the morning winds. Another possible explanation is that diurnal changed in the vertical permittivity arising through the condensation effects. These two reasons explained the azimuthal asymmetry of the scattering coefficients.

B. Polarization-Conversion Ratio

Polarization is an inherent feature of the EM waves, representing the trajectory of electric field oscillation at some fixed point in space. The radar detects the target information by transmitting the EM waves and receiving the scattered echoes. In general, any EM wave scattered from the rough surface consists of two field components: one with the same polarization state as the incident wave called copolarized scattering and the other one is an orthogonal component to the polarization state of the incident wave called cross-polarized scattering. Due to the modulation of the incident wave by the target, the polarization state of the scattered wave is different from that of the incident wave, which is called depolarization. In this section, the PCR, which evaluates the polarization-conversion capability of the incident wave when it gets through the rough surface, is extracted.

To evaluate the performance of the polarization-conversion capability, the PCR for incident β-polarization is defined as follows:

$$\mathrm{PCR}_\beta = \frac{\left|\sigma^o_{\alpha\beta}\right|^2}{\left|\sigma^o_{\alpha\beta}\right|^2 + \left|\sigma^o_{\beta\beta}\right|^2} \quad (9)$$

where $\sigma^o_{\alpha\beta}$ represents the scattering coefficient with α-polarized scattering and β-polarized incidence, α and β can be either linear or circular polarization, and $\alpha \neq \beta$.

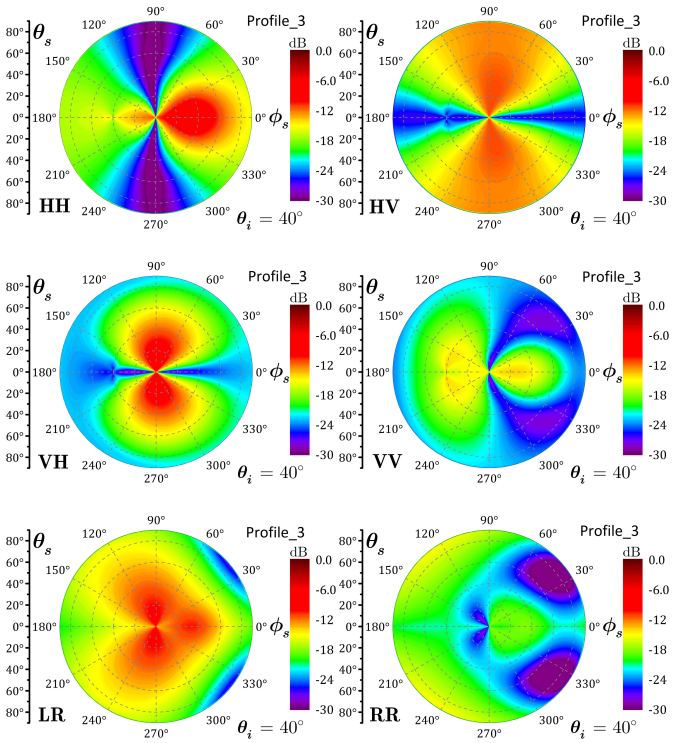

Fig. 5. Hemispherical plots of the linearly and circularly polarized bistatic scatterings on the scattering plane for the anisotropic inhomogeneous surfaces with profile_3, where the simulation parameters were set as $L_x = 5$ cm, $L_y = 20$ cm, $\sigma = 2$ cm, $\theta_i = 40°$, $\psi = 30°$, $f = 1.25$ GHz, and $\varepsilon_{rb} = 18 - j1.8$.

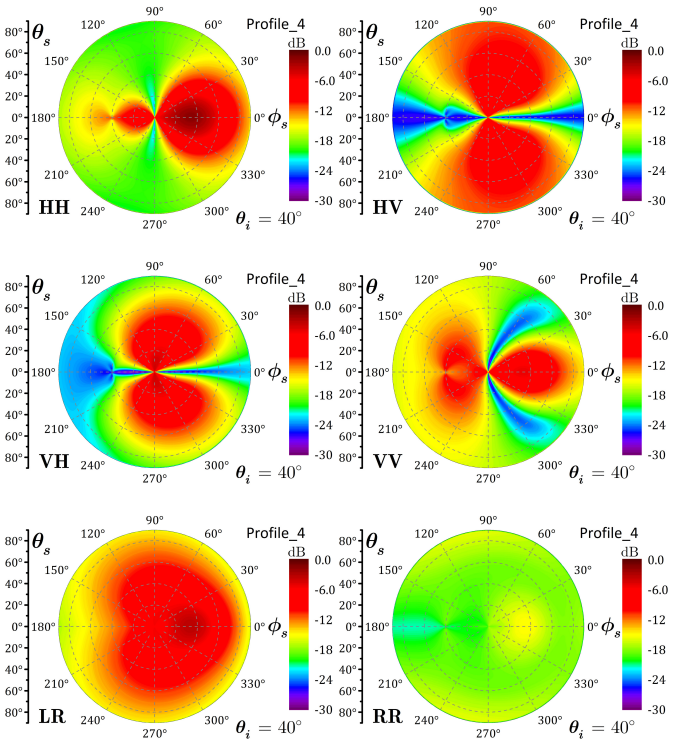

Fig. 6. Hemispherical plots of the linearly and circularly polarized bistatic scatterings on the scattering plane for the anisotropic inhomogeneous surfaces with profile_4, where the simulation parameters were set as $L_x = 5$ cm, $L_y = 20$ cm, $\sigma = 2$ cm, $\theta_i = 40°$, $\psi = 30°$, $f = 1.25$ GHz, and $\varepsilon_{rb} = 18 - j1.8$.

IV. Scattering From Anisotropic Inhomogeneous Surface

A. Bistatic Scattering Behaviors

In the previous section, an analytical model for predicting the fully polarized scattering behaviors of the anisotropic inhomogeneous rough surfaces was obtained. Here, data simulations are carried out to investigate the scattering properties for the rough surface with different dielectric profiles. To comprehend better the characteristics of the extracted PCR, the linearly and circularly polarized bistatic scatterings are first analyzed. In this section, for numerical illustration, taking two typical dielectric profiles with the same background dielectric constant (profile_3 and profile_4) as examples, the fully polarized bistatic scattering on the whole scattering plane is investigated. In both cases, correlation length $L(\psi)$ varies as the azimuthal angle, and dielectric constant $\varepsilon_r(z)$ is a function of depth. For numerical explanation, the correlation lengths along two vertical directions are assumed as $L_x = 5$ cm and $L_y = 20$ cm, and the rms height is fixed at 2 cm with the exponential correlated function and the frequency of 1.25 GHz. The background dielectric constant of the anisotropic inhomogeneous surfaces is $18 - j1.8$ for profile_3 and profile_4. The incident angle is set to 40°, and the view azimuthal angle is chosen at 40°. We show the hemispherical plots of the linearly and circularly polarized bistatic scatterings on the scattering plane for the anisotropic inhomogeneous surfaces with profile_3 in Fig. 5 and with profile_4 in Fig. 6. The scattering polar and azimuthal angles each vary with a step of 1°. Both for these two cases note that the linearly polarized scattering reveals stronger directional dependence, while the circularly polarized scattering tends to be more omnidirectional. For a rough surface with dielectric inhomogeneity and spatial anisotropy, the strong scattering region of HH polarization lies in around the specular direction. However, for VV polarization, the strong scattering region is more diffused in the backward region but contracted in the forward region. The deep scattering valley across the scattering polar angle appears at the cross-plane ($\phi_s = \pm 90°$) for HH polarizations, whereas for VV polarization, it is not so strict at the cross direction but instead tends to be in the forward region ($\phi_s = 60°, 300°$). For the HV and VH polarizations, the scattering coefficients are clustered in the cross-plane but their scattering behaviors are quite different. We find that the HV polarization is more dispersed in the scattering polar direction, while the strong scattering of VH polarization is more clustered to the low incidences. The scattering valley of HV and VH polarizations occurs in the incident plane ($\phi_s = 0°$), especially in the large scattering polar angle region. Namely, the depolarization effect is relatively weak in the incident plane. In addition, we would like to mention that the circular polarization tends to be more omnidirectional, and RR polarization is relatively smaller than RR polarization in general. By comparing Fig. 5 with Fig. 6, we found that although the background dielectric constants of profile_3 and profile_4 are the same, the differences in the bistatic scattering characteristics on the scattering plane are obvious. The bistatic scattering coefficients for the anisotropic inhomogeneous

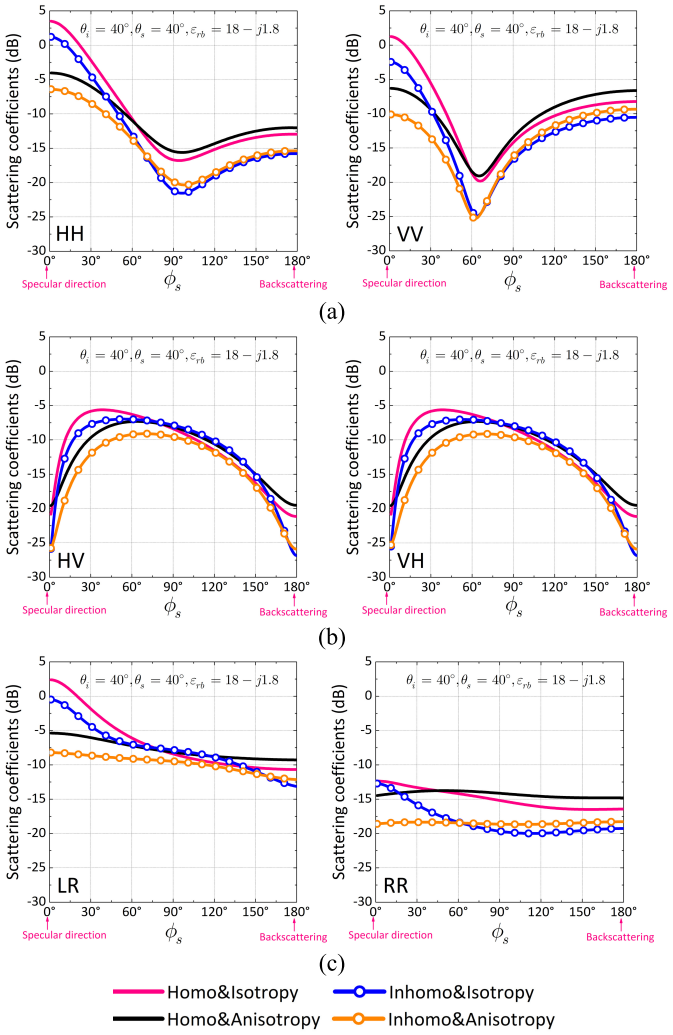

Fig. 7. Difference of bistatic scattering along the azimuthal direction for isotropic homogeneous, isotropic inhomogeneous, anisotropic homogeneous, and anisotropic inhomogeneous, respectively. The simulation parameters are $\sigma = 2$ cm, $\theta_i = 40°$, $\theta_s = 40°$, $\psi = 5°$, $f = 1.25$ GHz, $L_x = 5$ cm, $L_y = 20$ cm(anisotropic), $L_e = 12.5$ cm(isotropic), $\varepsilon_r = 18 - j1.8$ (homogenous), $\varepsilon_{rb} = 18 - j1.8$, and profile_4 (inhomogeneous). (a) Linear copolarizations HH and VV. (b) Linear cross-polarizations VH and HV. (c) Circular polarizations RR and LR.

surfaces with profile_4 are relatively greater than that with profile_3. This phenomenon can be well explained by the reflection behaviors in Fig. 2.

B. Sensitivity to Inhomogeneity and Anisotropy

Fig. 7 plots the bistatic scattering coefficients along the azimuthal direction for profile_4, where the differences among isotropic homogeneous, isotropic inhomogeneous, anisotropic homogeneous, and anisotropic inhomogeneous are indicated with $\sigma = 2$ cm, $\theta_i = 40°$, $\theta_i = 20°$, $\psi = 5°$, and $f = 1.25$ GHz. As a reference, we also plot the scattering coefficients for the isotropic homogeneous surfaces with the same background dielectric constant $(18 - j1.8)$ and the equivalent correlation length (12.5 cm) of the anisotropic surface ($L_x = 5$ cm, $L_y = 20$ cm). The bistatic scattering coefficients are weakened here due to the presence of inhomogeneity, along the azimuthal direction, and are more so at

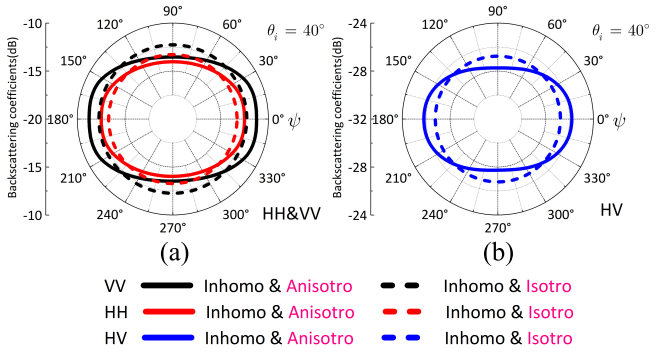

Fig. 8. Difference of backscattering between the isotropic inhomogeneous and anisotropic inhomogeneous surfaces. The simulation parameters are $\sigma = 2$ cm, $\theta_i = 40°$, $f = 1.25$ GHz, $L_x = 5$ cm, $L_y = 20$ cm (anisotropic), $L_e = 12.5$ cm(isotropic), $\varepsilon_r = 18 - j1.8$(homogenous), $\varepsilon_{rb} = 18 - j1.8$, and profile_4 (inhomogeneous). (a) Copolarizations HH and VV. (b) Linear cross-polarization HV.

the copolarization, particularly around the dip locations. The azimuthal angular trend of the circularly polarized scattering coefficient is flatter than that of linear polarization. The variations in the scattering strength for circular polarizations, both co- and cross-polarizations, are quite small.

Looking into more detail reveals that the spatial anisotropy has less impact on the linearly and circularly polarized scatterings except for specular direction and its vicinity, regardless of the surface being homogeneous or inhomogeneous. From the above observations, it is inferred that the bistatic scattering coefficients in the azimuth direction are more sensitive to dielectric inhomogeneity than to spatial anisotropy. The effect of anisotropy is more pronounced around the specular scattering direction. Among these four rough surface cases, the dielectric inhomogeneity and spatial anisotropy jointly exercise more influence, and the difference in bistatic scattering between the isotropic homogeneous and the anisotropic inhomogeneous is even more pronounced. It is worth noting at this point that the scattering pattern in terms of scattering strength level and angular trend will be complex when we vary the degree of spatial anisotropy and dielectric inhomogeneity, since their coupling effect may enhance or diminish the scattering coefficient. Such a dependence will be investigated in the whole scattering plane.

We investigate the scattering from the anisotropic and isotropic inhomogeneous rough surfaces in the backscattering and specular scattering directions in Figs. 8 and 9, respectively. In Figs. 8 and 9, the solid lines represent the anisotropic cases and the dashed lines represent the isotropic cases. It is clear that with including the anisotropy, we can better capture the characteristics of azimuthal dependence compared with the circular curves that are from the isotropic surface indicating azimuth-independent. By comparison, the specular scattering coefficients are more sensitive to the spatial anisotropy, especially at $\psi = 0°, 180°$, in which the difference due to anisotropy is as large as 8 dB. The effect of anisotropy between backscattering and specular scattering is similar in cross-polarization but that is quite different in copolarization. Note that, due to the anisotropy, the backscattering coefficients increase but the specular scattering coefficients decrease for

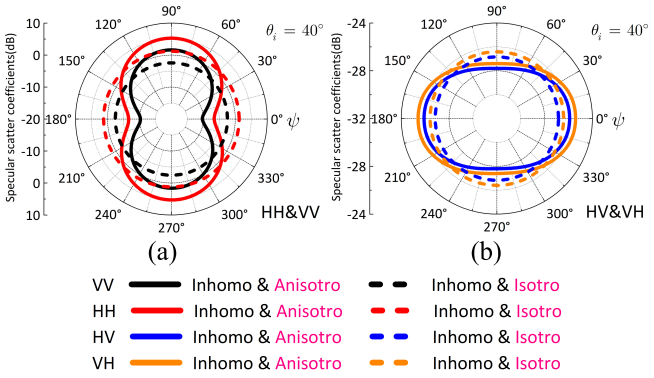

Fig. 9. Difference in specular scattering between the isotropic inhomogeneous and anisotropic inhomogeneous surfaces. The simulation parameters are $L_x = 5$ cm, $L_y = 20$ cm(anisotropic), $L_e = 12.5$ cm(isotropic), $\varepsilon_r = 18 - j1.8$(homogenous), $\varepsilon_{rb} = 18 - j1.8$, and profile_4 (inhomogeneous). (a) Copolarizations HH and VV. (b) Linear cross-polarizations HV and VH.

the azimuth ranges of $0° \le \psi \le 45°, 135° \le \psi \le 180°$; however, the trend is reverse where $45° \le \psi \le 135°$. From the above observations, it is inferred that the spatial anisotropy cannot be neglected for rough surface scattering, especially at the specular direction.

We now examine the sensitivity of bistatic scattering to the dielectric inhomogeneity and spatial anisotropy. Note that the effects of dielectric inhomogeneity and spatial anisotropy on bistatic scattering can be weakening or enhancing the scattering strength. In Fig. 10, the scattering is weaker from anisotropic inhomogeneous than from isotropic homogeneous surfaces at the H-polarized incidence, as is seen in both HH and VH polarizations, that is, for H-polarized incidence, the effect of inhomogeneity and anisotropy on the bistatic scattering to reduce the scattering. For V-polarized incidence, things change. In detail, for VV polarization, we note that the scattering coefficients are enhanced along the scattering polar direction but weakened around the incident plane. For depolarized HV polarization, the effect is to enhance the scattering around a scattering angle of 40° when the scattering azimuth angle lies in between 135° and 225°. By comparison, the copolarization is more sensitive to the presence of dielectric inhomogeneity and spatial anisotropy than cross-polarization is. It becomes apparent that at the V-polarized incidence, the dynamic range increases due to the presence of dielectric inhomogeneity and spatial anisotropy. For circular polarization, the dynamic range of the scattering strength due to dielectric inhomogeneity and spatial anisotropy is greater in LR polarization than in RR polarization, that is, the LR polarization is more sensitive to the dielectric inhomogeneity and spatial anisotropy.

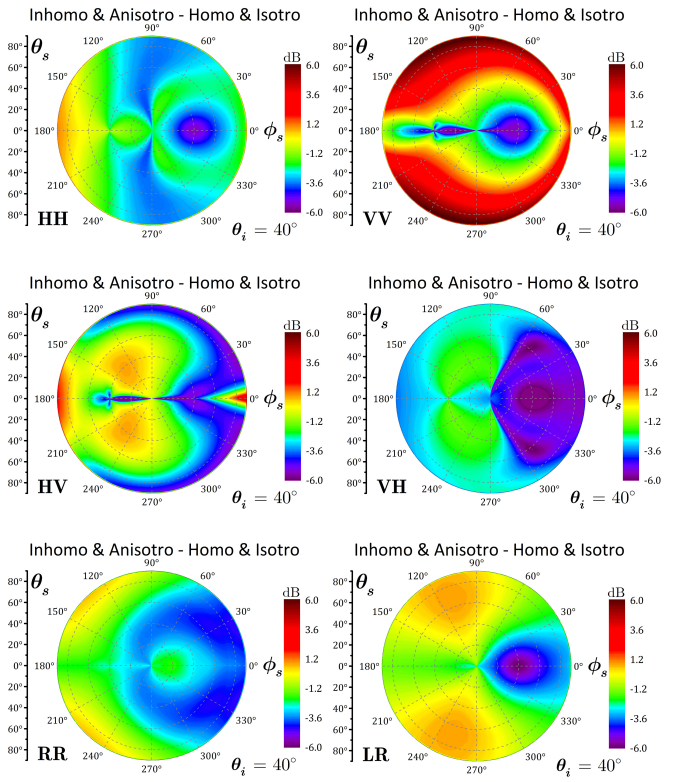

Fig. 10. Difference of bistatic scattering on the scattering plane between the anisotropic inhomogeneous and isotropic homogeneous surfaces. The simulation parameters are $\sigma = 2$ cm, $\theta_i = 40°, \psi = 30°$, and $f = 1.25$ GHz, $\varepsilon_{rb} = 18 - j1.8$. For anisotropic inhomogeneous: $L_x = 5$ cm, $L_y = 20$ cm, and profile_4. For isotropic homogeneous: $L_e = 12.5$ cm.

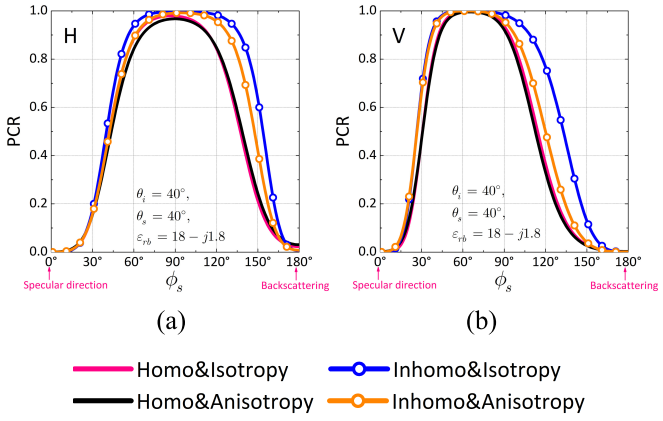

Fig. 11. PCR along the azimuthal direction for isotropic homogeneous, isotropic inhomogeneous, anisotropic homogeneous, and anisotropic inhomogeneous, respectively. The simulation parameters are $\sigma = 2$ cm, $\theta_i = 40°, \theta_s = 40°, \psi = 5°$, and $f = 1.25$ GHz, $L_x = 5$ cm, $L_y = 20$ cm(anisotropic), $L_e = 12.5$ cm(isotropic), $\varepsilon_r = 18 - j1.8$ (homogenous), $\varepsilon_{rb} = 18 - j1.8$, and profile_4 (inhomogeneous). (a) H-polarized incidences. (b) V-polarized incidences.

V. Results and Discussion

In this section, the examination of the different dielectric profile, surface parameter (inhomogeneity, anisotropy, rms height, and background dielectric constant), and radar parameter (incident angle) effects on the PCR is in order.

In Fig. 11, we investigate the PCR along the azimuthal direction for isotropic homogeneous, isotropic inhomogeneous, anisotropic homogeneous, and anisotropic inhomogeneous, respectively. The simulation parameters are the same as that shown in Fig. 7. Note that the PCR increases first and then decreases in the azimuth direction, that is, in the forward scattering region, the PCR is enhanced as the azimuthal angle increases; however, in the backward scattering region, the PCR is weakened with the azimuthal angle increasing. The highest PCR occurs in the cross

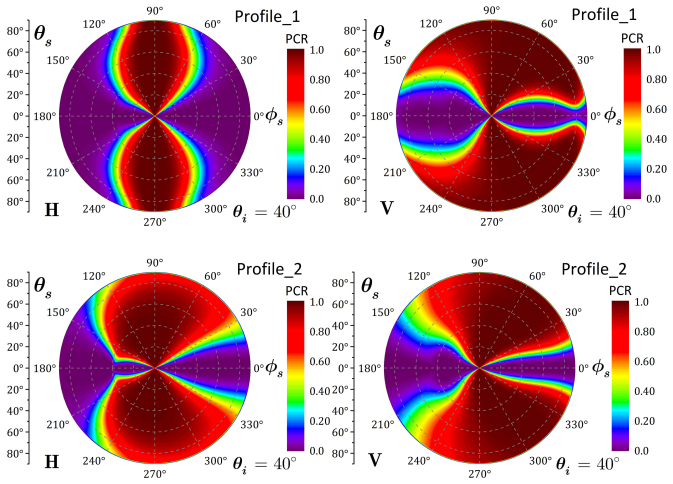

Fig. 12. PCR plots on the scattering plane for anisotropic inhomogeneous surfaces with profile_1 and profile_2. The simulation parameters were set as $L_x = 5$ cm, $L_y = 20$ cm, $\sigma = 2$ cm, $\theta_i = 40°$, $\psi = 30°$, and $f = 1.25$ GHz, $\varepsilon_{rb} = 4.5 - j0.45$, $\varepsilon_{r\max} = 20 - j2.0$.

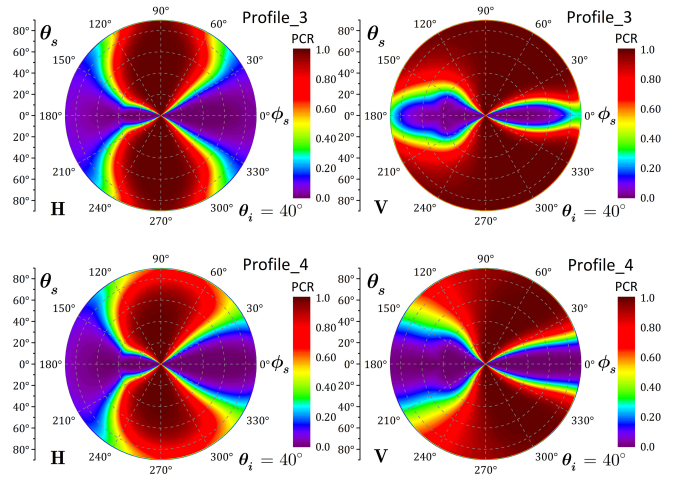

Fig. 13. PCR plots on the scattering plane for anisotropic inhomogeneous surfaces with profile_3 and profile_4. The simulation parameters were set as $L_x = 5$ cm, $L_y = 20$ cm, $\sigma = 2$ cm, $\theta_i = 40°$, $\psi = 30°$, and $f = 1.25$ GHz$\varepsilon_{rb} = 18 - j1.8$.

direction ($\phi_s = 90°$). Here, we also point out the PCR in two common directions: backscattering and specular scattering directions. We note that the PCR is almost 0 in these two directions, which suggests that the polarization of the incident wave is rarely converted into the backscattering and specular scattering directions by the rough surfaces. In addition, the PCR is more sensitive to the anisotropy and inhomogeneity in the backward scattering region.

A. PCR for Different Dielectric Profiles

Two sets of dielectric profiles are considered here: 1) profile_1 and profile_2 with the same maximum permittivity of $20 - j2.0$ and background permittivity of $4.45 - j0.45$ and 2) profile_3 and profile_4 with the same background permittivity of $18 - j1.8$, as shown in Figs. 12 and 13. These are a significant example, because, as already mentioned in Section II, the anisotropic inhomogeneous surfaces are very common in the natural environment. The simulation parameters were set as $L_x = 5$ cm, $L_y = 20$ cm, $\sigma = 2$ cm, $\theta_i = 40°$, $\psi = 30°$, and $f = 1.25$ GHz. To investigate further the polarization dependence of the incident wave, both the vertically and horizontally polarized incidences are explored. Visual inspections of Figs. 12 and 13 reveal that depolarized scattering patterns with different polarization states of incident waves are quite different. The PCR is more clustered in the cross-plane for horizontally polarized incidence. However, for vertically polarized incidence, the PCR disperses resembling "fan-beam" on the whole scattering plane with sharp valley occurring in the incident plane. By comparison, the strong PCR area with vertically polarized incidence is larger than that with horizontally polarized incidence. That is to say that the polarization-conversion capability is relatively stronger at the vertically polarized incidence. In addition, compared with Figs. 12 and 13, we readily acknowledge that the distribution of the PCR on the whole scattering plane varies for different dielectric structures. Here, we examine the PCR plots on the scattering plane for different dielectric profiles but with the same background permittivity. In Fig. 12, the hemispherical plots of the PCR for dielectric profile_1 and profile_2 are compared. As shown in Fig. 2(a1), profile_1 and profile_2 have the same maximum and background dielectric constants, but the depths of the maximum dielectric constants are different. Under this dielectric structure, as the maximum dielectric constants decrease, the strong PCR area enlarges and moves to the forward scattering for horizontally polarized incidence, but slightly narrow in backward scattering for vertically polarized incidence. In Fig. 13, we investigate the PCR for two monotonic dielectric profiles (profile_3 and profile_4) with the same background permittivity but different variation paths. The PCR is relatively weak when the slope of the dielectric profile gradually increases. In summary, the PCR is affected by both the change rate of the dielectric profile and the background dielectric constant, namely, the different anisotropic inhomogeneous surface structures can convert polarization efficiently in the cross-plane for H-polarized incidence but in scattering plane except for the incident plane for V-polarized incidence. The effect of background permittivity for the same dielectric profiles on the PCR will be explored in Section V-B.

B. Effect of Surface and Radar Parameters

In Fig. 14, we investigate the bistatic scattering coefficients and the PCR varying with the degree of inhomogeneity for the anisotropic inhomogeneous surface. From Fig. 14(a) and (b), we can see that both co- and cross-polarized scattering coefficients are enhanced as the degree of inhomogeneity. Fig. 4(c) illustrates that, for the same dielectric profile, the change in the PCR is not significant as the degree of inhomogeneity increases. The PCR for different dielectric profiles has been given in Figs. 12 and 13.

To examine further the impacts of inhomogeneity on the PCR, numerical results are analyzed for both vertically and horizontally polarized incidences, as shown in Fig. 15. The PCR for anisotropic homogeneous and inhomogeneous surfaces is shown in Fig. 15(a) and (b), and their difference is given in Fig. 15(c). Note that the inhomogeneity has a

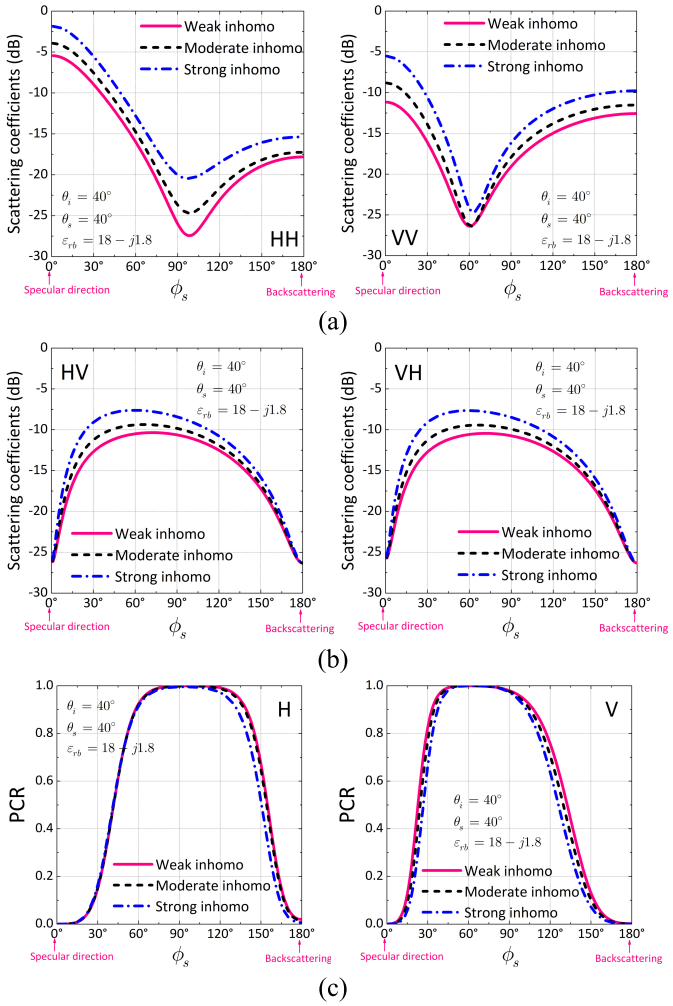

Fig. 14. Bistatic scattering coefficients and PCR vary with the degree of inhomogeneity for anisotropic inhomogeneous surface. The simulation parameters are $L_x = 5$ cm, $L_y = 20$ cm, $\sigma = 2$ cm, $\varepsilon_{rb} = 18 - j1.8$, $\theta_i = 40°$, $\theta_s = 40°$, $\psi = 30°$, and $f = 1.25$ GHz, and profile_4. (a) Linear copolarizations HH and VV. (b) Linear cross-polarizations VH and HV. (c) PCR for the H-polarized and V-polarized incidences.

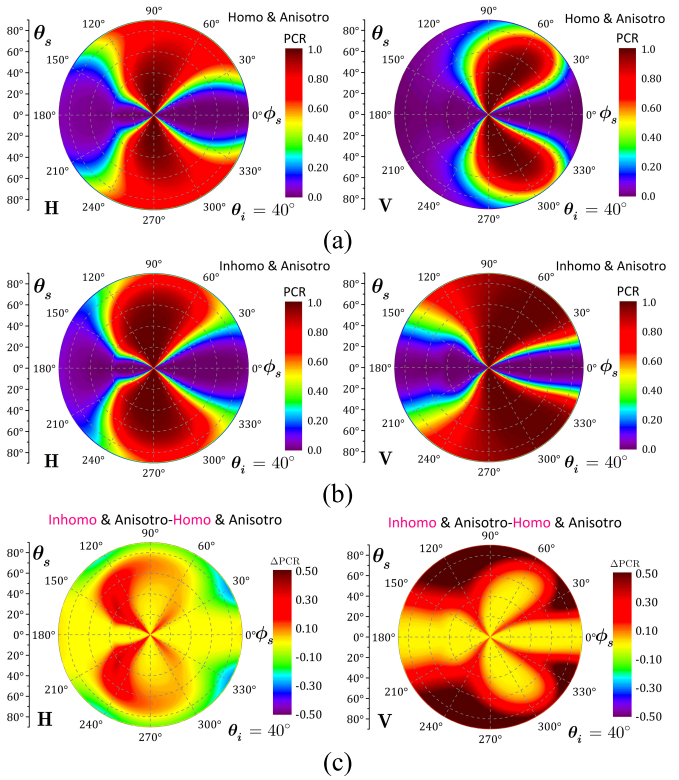

Fig. 15. Effects of inhomogeneity on PCR in the whole scattering plane for profile_4. The simulation parameters were set as $L_x = 5$ cm, $L_y = 20$ cm, $\sigma = 2$ cm, $\theta_i = 40°$, $\psi = 30°$, and $f = 1.25$ GHz, $\varepsilon_{rb} = 18 - j1.8$. (a) Anisotropic homogeneous surface. (b) Anisotropic inhomogeneous surface. (c) Difference in PCR between the anisotropic homogeneous and inhomogeneous surfaces.

significant influence on the PCR, especially at the vertically polarized incidence. Due to the inhomogeneity, the PCR at the horizontally polarized incidence gradually converges but enhances in the cross-plane. However, at the vertically polarized incidence, the PCR distribution progressively disperses over the backward region. Note that the PCR is more sensitive to inhomogeneity at the vertically polarized incidence, and the inhomogeneity enables to convert polarization more efficiently in the cross-plane at both H-polarized and V-polarized incidences. From Fig. 15(c), we see that the effect of inhomogeneity on the PCR in the whole scattering plane is to enhance the scattering at the vertically polarized incidence, but is to diminish the scattering at a larger scattering angle at the horizontally polarized incidence, that is, at a larger scattering angle region, the polarization-conversion capability increases at the vertically polarized incidence but decreases at the horizontally polarized incidence by the presence of dielectric inhomogeneity.

Fig. 16 shows the specular scattering coefficients varying with the degree of anisotropy. At the first glance, as the anisotropic azimuthal angle increases, the linearly copolarized scattering coefficients increase first and then decrease. However, the trend of cross-polarized scattering is reversed. Meanwhile, with the degree of anisotropy increasing, the copolarized scattering coefficients are weakened overall and the azimuth dependence becomes stronger, whereas the cross-polarized scattering coefficients are entirely enhanced.

Next, we examine the effect of anisotropy on the PCR shown in Fig. 17. The PCR on the whole scattering plane for the isotropic and anisotropic inhomogeneous surfaces is shown in Fig. 17(a) and (b), and their difference with the anisotropic view azimuthal angle of 60° is displayed in Fig. 17(c). From Fig. 17(a) and (b), the region of strong PCR is reduced for the anisotropic inhomogeneous surface. From Fig. 17(c), it is evident that the PCR decreases due to spatial anisotropy when $\psi = 5°$, and this reduction is more pronounced in the backward scattering region, that is, the effect of spatial anisotropy on the PCR is greater in the backward scattering region at both horizontally and vertically polarized incidences. The above analysis suggests that the spatial anisotropy weakens the polarization-conversion capability in the backward scattering region.

In Figs. 18 and 19, we investigate the backscattering and specular scattering coefficient as a function of the background moisture content and the rms height for the anisotropy inhomogeneous surface, respectively. The simulation parameters were set as $L_x = 5$ cm, $L_y = 20$ cm, $\psi = 30°$, $\varepsilon_{rb} = 9 - j0.9$,

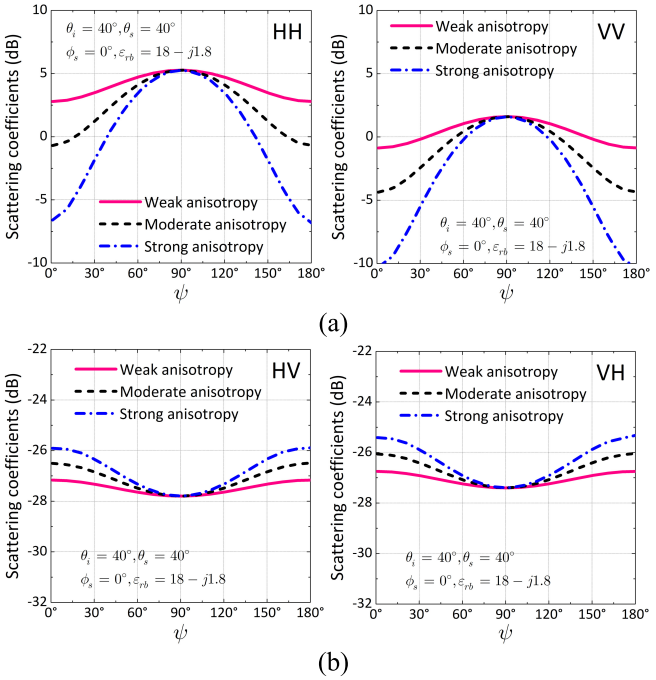

Fig. 16. Specular scattering coefficients vary with the degree of anisotropy for the anisotropic inhomogeneous surface. The simulation parameters are $L_x = 5, 10, 15$ cm, $L_y = 20$ cm, $\sigma = 2$ cm, $\varepsilon_{rb} = 18 - j1.8$, $\theta_i = 40°$, $\theta_s = 40°$, $\phi_s = 0°$, and $f = 1.25$ GHz, and profile_4. (a) Linear copolarizations HH and VV. (b) Linear cross-polarizations VH and HV.

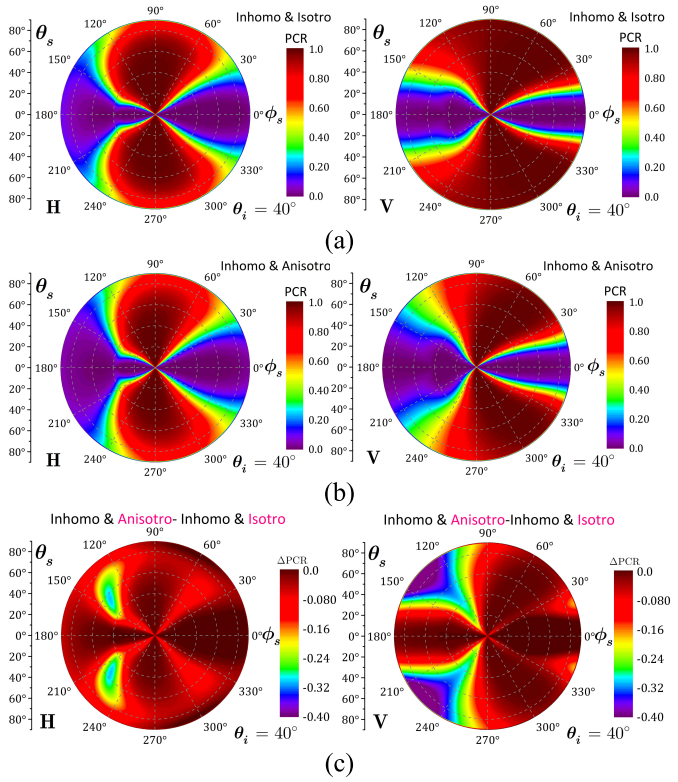

Fig. 17. Effects of anisotropy on PCR in the whole scattering plane for profile_4. The simulation parameters were set as $L_x = 5$ cm, $L_y = 20$ cm, $\psi = 5°$ (anisotropic), $L_e = 12.5$ cm (isotropic), $\sigma = 2$ cm, $\theta_i = 40°$, and $f = 1.25$ GHz, $\varepsilon_{rb} = 18 - j1.8$. (a) Isotropic inhomogeneous surface. (b) Anisotropic inhomogeneous surface. (c) Difference in PCR between the isotropic inhomogeneous and anisotropic inhomogeneous surfaces.

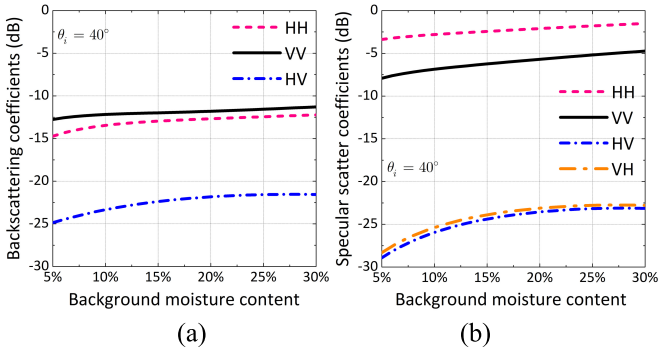

Fig. 18. Backscattering and specular scattering coefficient as a function of background moisture content for the anisotropy inhomogeneous surface with profile_4 in the whole scattering plane. The simulation parameters were set as $L_x = 5$ cm, $L_y = 20$ cm, $\psi = 30°, \varepsilon_{rb} = 9 - j0.9, \theta_i = 40°$, $f = 1.25$ GHz. (a) Backscattering coefficients $\phi_s = 180°$. (b) Specular scattering coefficients $\phi_s = 0°$.

$\theta_i = 40°$, and $f = 1.25$ GHz. From Fig. 18, we note that both backscattering and specular scattering coefficients increase slightly, as the background moisture content increases. From Fig. 19, with the increase in rms height, both backscattering and specular scattering coefficients increase first and then flatten out. Apart from this, we can see that the cross-polarized scattering decreases for large rms height. In addition, VV polarized scattering is larger than HH polarization in backscattering, but it is less than HH in the specular scattering direction. The VH and HV polarizations are close, and VH is slightly larger than HV polarization.

The background dielectric constant and rms height are two key surface parameters to describe the reflection and scattering behaviors. In what follows, we investigate the impact of the background dielectric and the rms height on the PCR in the whole scattering plane in Figs. 20 and 21, respectively. As shown in Fig. 20, taking profile_4 as an example, we investigate the difference in PCR with a background dielectric constant of $18 - j1.8$ and $9 - j0.9$. The results show that the surface structures with different background dielectric constants have a great impact on the polarization-conversion efficiency. As the background dielectric constant increases, for horizontally polarized incidence, the PCR is reduced in the cross-plane, but enhanced in the backward and forward regions with a large scattering angle. However, for vertically polarized incidence, the increase in the background dielectric constant enhances the polarization-conversion capability in the incident plane and the forward region. In Fig. 21, we illustrate the difference between the PCRs when the rms height varies from 1 to 3 cm. Unlike other surface parameters, as the rms height increases, the impacts of rms height on the PCR are negative on the whole scattering plane. We note that the PCR is obliviously affected in the cross-plane with a large scattering angle for the horizontally polarized incidence. However, for the vertically polarized incidence, the PCR is greatly affected by the rms height in the forward scattering region except the incident plane.

In Fig. 22, we give the effect of incident angle on the PCR for the anisotropic inhomogeneous rough surfaces in the whole scattering plane. For numerical illustration, profile_4 with a

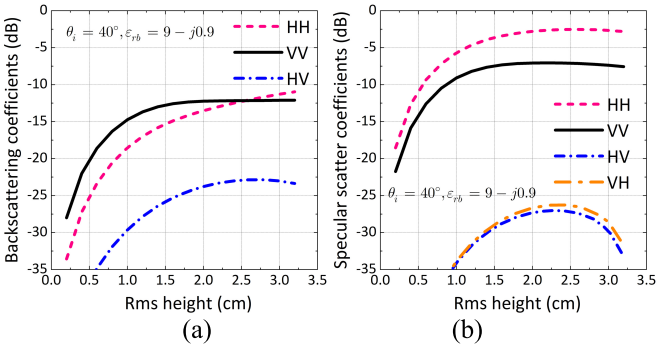

Fig. 19. Backscattering and specular scattering coefficient as a function of rms height for the anisotropy inhomogeneous surface with profile_4 in the whole scattering plane. The simulation parameters were set as $L_x = 5$ cm, $L_y = 20$ cm, $\psi = 30°, \varepsilon_{rb} = 9 - j0.9 \theta_i = 40°$, and $f = 1.25$ GHz. (a) Backscattering coefficients $\phi_s = 180°$. (b) Specular scattering coefficients $\phi_s = 0°$.

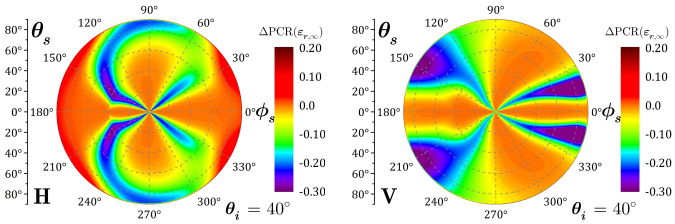

Fig. 20. Effects of background dielectric constant on PCR for the anisotropy inhomogeneous surface with profile_4 in the whole scattering plane. The simulation parameters were set as $L_x = 5$ cm, $L_y = 20$ cm, $\sigma = 2$ cm, $\theta_i = 40°, \psi = 30°$, and $f = 1.25$ GHz, and $\Delta\varepsilon_{r\infty} = (18 - j1.8) - (9 - j0.9)$.

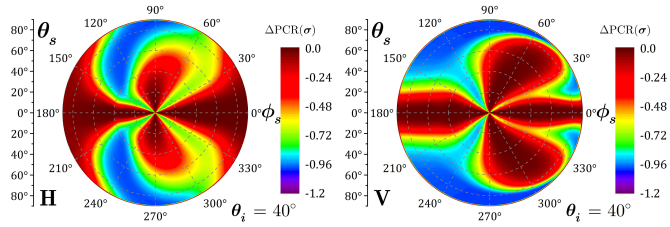

Fig. 21. Effects of rms height on PCR for the anisotropy inhomogeneous surface with profile_4 in the whole scattering plane. The simulation parameters were set as $L_x = 5$ cm, $L_y = 20$ cm, $\theta_i = 40°, \psi = 30°, \varepsilon_{r\infty} = 18 - j1.8$, and $f = 1.25$ GHz. $\sigma = 3$ cm $- 1$ cm.

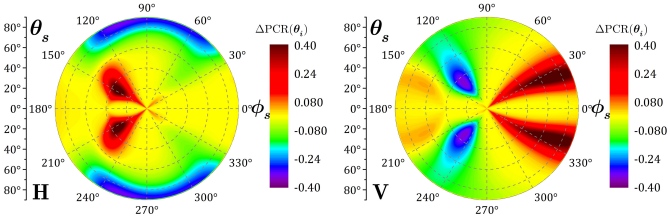

Fig. 22. Effect of incident angle on PCR in the whole scattering plane for the anisotropic inhomogeneous surfaces with profile_4. The simulation parameters are $L_x = 5$ cm, $L_y = 20$ cm, $\sigma = 2$ cm, $\psi = 30°$, and $f = 1.25$ GHz, $\varepsilon_{rb} = 18 - j1.8, \theta_i = 20°, 40°$.

background permittivity of $18 - j1.8$ is taken as an example here. The incident angles are selected as 20° and 40°. The simulation parameters were $L_x = 5$ cm, $L_y = 20$ cm, $\sigma = 2$ cm, $\psi = 30°$. The frequency is 1.25 GHz. Note that the effects of incident angle on the whole scattering plane are positive or negative. At a smaller scattering angle, when the scattering azimuthal angle varies from 120° to 150° and 210° to 240°, the increase in the incident angle effectively prompts the polarization-conversion capability for the horizontally polarized incidence but reduces it for the vertically polarized incidence. In addition, as the incident angle increases, the PCR is enhanced in the forward region with the scattering azimuthal angle around 30° and 330°.

Before closing this section, we emphasize that following the formation of spatial anisotropy in the agriculture field, for instance, the moisture content of the soil surface is keenly dependent on the vertical depth due to the evapotranspiration process—wet-down or dry-up. It would be more general to treat such a soil surface as the anisotropic and inhomogeneous rough surface. In modeling the scattering, the subsurface can be equivalently treated as a multilayer medium in virtue of dielectric inhomogeneity. By applying the boundary condition at each layer, the complex reflection coefficients of the rough surface on the top of the medium can be solved recursively by accounting for the subsurface reflections and refractions. For different dielectric profiles, the angular dependence of the reflection coefficients varies accordingly, so are the scattering features. Thus, the surface roughness varies with the view azimuthal angle and depends on the degree of anisotropy. The scattering modulation appears in the view azimuth direction due to the anisotropy. The reason for this modulation is perhaps due to the scattering reduction in these ridged structures when the view azimuth angles are 0° and 180°.

VI. Conclusion

The PCR for the scattering of the rough surface with dielectric inhomogeneity and spatial anisotropy is investigated. Numerical results show that the patterns of the PCR on the whole scattering plane for the anisotropic inhomogeneous rough surfaces with different dielectric profiles are quite similar. The polarization states of the incident waves greatly affect the polarization-conversion capability. We note that the PCR is more clustered in the cross-plane for the horizontally polarized incidence. However, for the vertically polarized incidence, the PCR disperses resembling "fan-beam" on the whole scattering plane with a sharp valley occurring in the incident plane. The distribution of a strong PCR region on the whole scattering plane varies on different dielectric profiles. The inhomogeneity has a great influence on the PCR, especially at the vertically polarized incidence. The inhomogeneity converts polarization efficiently in the cross-plane for both H-polarized and V-polarized incidences. At larger scattering regions, the dielectric inhomogeneity increases the polarization-conversion capability for the vertically polarized incidence but reduces it for the horizontally polarized incidence. The PCR is stronger in cross-plane with a large scattering angle for the horizontally polarized incidence, but in a backward scattering region for the vertically polarized incidence. The polarization of the incident wave is rarely converted in the backscattering and specular scattering directions by the rough surfaces. The PCR is more sensitive to the dielectric inhomogeneity than that to spatial anisotropy. As the background dielectric constant increases, for the horizontally

polarized incidence, the PCR is reduced in the cross-plane but enhanced in the backward and forward regions with a large scattering angle. However, at the vertically polarized incidence, the increase in the background dielectric constant enhances the polarization-conversion capability in the incident plane and the forward region. With the increasing incident angle, the stronger PCR appears in the backward region at the horizontally polarized incidence but in the forward region at the vertically polarized incidence. In all numerical illustrations, the coupling effects of spatial anisotropy and dielectric inhomogeneity are complex, and each exercises different impacts on scattering, either in forward or backward scattering. Results demonstrate that the PCR offers an effective measure to identify the effects of spatial anisotropy and dielectric inhomogeneity.

REFERENCES

[1] L. Tsang, J. A. Kong, and R. T. Shin, *Theory of Microwave Remote Sensing*, New York, NY, USA: Wiley, 1985.

[2] A. K. Fung, *Microwave Scattering and Emission Models and Their Applications*. Norwell, MA, USA: Artech House, 1994.

[3] J. S. Lee, *Polarimetric Radar Imaging: From Basics To Applications*. Boca Raton, FL, USA: CRC Press, 2009.

[4] G. Liu *et al.*, "A systematic comparison of the effect of polarization ratio models on sea surface wind retrieval from C-band synthetic aperture radar," *IEEE J. Sel. Topics Appl. Earth Observ. Remote Sens.*, vol. 6, no. 3, pp. 1100–1108, Jun. 2013.

[5] K. S. Min, J. Hirokawa, K. Sakurai, M. Ando, and N. Goto, "Single-layer dipole array for linear-to-circular polarisation conversion of slotted waveguide array," *IEE Proc.-Microw., Antennas Propag.*, vol. 143, no. 3, pp. 211–216, Jun. 1996.

[6] J. Wang *et al.*, "Super-thin cloaks mediated by spoof surface plasmons," *Photon. Nanostruct.-Fundam. Appl.*, vol. 10, no. 4, pp. 540–546, Oct. 2012.

[7] J. Lee, M. Yoo, and S. Lim, "A study of ultra-thin single layer frequency selective surface microwave absorbers with three different bandwidths using double resonance," *IEEE Trans. Antennas Propag.*, vol. 63, no. 1, pp. 221–230, Jan. 2015.

[8] M. I. Khan and F. A. Tahir, "An angularly stable dual-broadband anisotropic cross polarization conversion metasurface," *J. Appl. Phys.*, vol. 122, no. 5, Aug. 2017, Art. no. 053103.

[9] M. I. Khan, Z. Khalid, and F. A. Tahir, "Linear and circular-polarization conversion in X-band using anisotropic metasurface," *Sci. Rep.*, vol. 9, no. 1, p. 4552, Dec. 2019.

[10] N. K. Grady *et al.*, "Terahertz metamaterials for linear polarization conversion and anomalous refraction," *Science*, vol. 340, no. 6138, pp. 1304–1307, May 2013.

[11] P. E. Sieber and D. H. Werner, "Infrared broadband quarter-wave and half-wave plates synthesized from anisotropic Bézier metasurfaces," *Opt. Express*, vol. 22, no. 26, pp. 32371–32383, 2014.

[12] F. Qin *et al.*, "Hybrid bilayer plasmonic metasurface efficiently manipulates visible light," *Sci. Adv.*, vol. 2, no. 1, Jan. 2016, Art. no. e1501168.

[13] J. Lončar, A. Grbic, and S. Hrabar, "A reflective polarization converting metasurface at X-band frequencies," *IEEE Trans. Antennas Propag.*, vol. 66, no. 6, pp. 3213–3218, Jun. 2018.

[14] S. Bhattacharyya, S. Ghosh, and K. V. Srivastava, "A wideband cross polarization conversion using metasurface," *Radio Sci.*, vol. 52, no. 11, pp. 1395–1404, Nov. 2017.

[15] E. Doumanis, G. Goussetis, J. L. Gomez-Tornero, R. Cahill, and V. Fusco, "Anisotropic impedance surfaces for linear to circular polarization conversion," *IEEE Trans. Antennas Propag.*, vol. 60, no. 1, pp. 212–219, Jan. 2012.

[16] L. M. Brekhovskikh, *Waves in Layered Media*, R.T. Beyer, Ed., 2nd ed. New York, NY, USA: Academic, 1980.

[17] E. G. Njoku and J.-A. Kong, "Theory for passive microwave remote sensing of near-surface soil moisture," *J. Geophys. Res.*, vol. 82, no. 20, pp. 3108–3118, Jul. 1977.

[18] J. Cihlar and F. T. Ulaby, "Dielectric properties of soils as a function of moisture content," Remote Sens. Lab., Lawrence, KS, USA, Tech. Rep. 177-47, 1974.

[19] J. Zeng, K.-S. Chen, H. Bi, T. Zhao, and X. Yang, "A comprehensive analysis of rough soil surface scattering and emission predicted by AIEM with comparison to numerical simulations and experimental measurements," *IEEE Trans. Geosci. Remote Sens.*, vol. 55, no. 3, pp. 1696–1708, Mar. 2017.

[20] M. Brogioni *et al.*, "Sensitivity of bistatic scattering to soil moisture and surface roughness of bare soils," *Int. J. Remote Sens.*, vol. 31, no. 15, pp. 4227–4255, Aug. 2010.

[21] S. Paloscia, P. Pampaloni, S. Pettinato, and E. Santi, "A comparison of algorithms for retrieving soil moisture from ENVISAT/ASAR images," *IEEE Trans. Geosci. Remote Sens.*, vol. 46, no. 10, pp. 3274–3284, Oct. 2008.

[22] W. A. Bereuter and D. C. Chang, "Electromagnetic remote sensing of inhomogeneous media," U.S. Dept. Commerce, Boulder, CO, USA, Tech, Rep., 1977.

[23] K. Sarabandi and T. Chiu, "Electromagnetic scattering from slightly rough surfaces with inhomogeneous dielectric profiles," *IEEE Trans. Antennas Propag.*, vol. 45, no. 9, pp. 1419–1430, Sep. 1997.

[24] S. A. Tabatabaeenejad and M. Moghaddam, "Bistatic scattering from dielectric structures with two rough boundaries using the small perturbation method," *IEEE Trans. Geosci. Remote Sens.*, vol. 44, no. 8, pp. 2102–2124, Aug. 2006.

[25] L. Tsang, K.-H. Ding, S. Huang, and X. Xu, "Electromagnetic computation in scattering of electromagnetic waves by random rough surface and dense media in microwave remote sensing of land surfaces," *Proc. IEEE*, vol. 101, no. 2, pp. 255–279, Feb. 2013.

[26] A. S. Komarov, L. Shafai, and D. G. Barber, "Electromagnetic wave scattering from rough boundaries interfacing inhomogeneous media and application to snow-covered sea ice," *Prog. Electromagn. Res.*, vol. 144, pp. 201–219, 2014.

[27] H. Zamani, A. Tavakoli, and M. Dehmollaian, "Scattering from two rough surfaces with inhomogeneous dielectric profiles," *IEEE Trans. Antennas Propag.*, vol. 63, no. 12, pp. 5753–5766, Dec. 2015.

[28] M. Sanamzadeh, L. Tsang, and J. T. Johnson, "3-D electromagnetic scattering from multilayer dielectric media with 2-D random rough interfaces using T-matrix approach," *IEEE Trans. Antennas Propag.*, vol. 67, no. 1, pp. 495–503, Jan. 2019.

[29] L. Bateson and I. H. Woodhouse, "Observations of scatterometer asymmetry over sand seas and derivation of wind ripple orientation," *Int. J. Remote Sens.*, vol. 25, no. 10, pp. 1805–1816, 2004.

[30] Z. Bartalis, K. Scipal, and W. Wagner, "Azimuthal anisotropy of scatterometer measurements over land," *IEEE Trans. Geosci. Remote Sens.*, vol. 44, no. 8, pp. 2083–2092, Aug. 2006.

[31] P. Xu *et al.*, "Full-wave simulation and analysis of bistatic scattering and polarimetric emissions from double-layered sastrugi surfaces," *IEEE Trans. Geosci. Remote Sens.*, vol. 55, no. 1, pp. 292–307, Jan. 2017.

[32] H.-J. He and L.-X. Guo, "Efficient hybrid method for electromagnetic scattering from a coated object above a two-layered rough surface," *Appl. Opt.*, vol. 57, no. 25, pp. 7102–7108, 2018.

[33] D. Comite and N. Pierdicca, "Monostatic and bistatic scattering modeling of the anisotropic rough soil," *IEEE Trans. Geosci. Remote Sens.*, vol. 57, no. 5, pp. 2543–2556, May 2019.

[34] A. K. Fung, Z. Li, and K. S. Chen, "Backscattering from a randomly rough dielectric surface," *IEEE Trans. Geosci. Remote Sens.*, vol. 30, no. 2, pp. 356–369, Mar. 1992.

[35] A. K. Fung, and K. S. Chen, *Microwave Scattering and Emission Models for Users*. Norwood, MA, USA: Artech House, 2010.

[36] K. S. Chen, T.-D. Wu, L. Tsang, Q. Li, J. Shi, and A. K. Fung, "Emission of rough surfaces calculated by the integral equation method with comparison to three-dimensional moment method simulations," *IEEE Trans. Geosci. Remote Sens.*, vol. 41, no. 1, pp. 90–101, Jan. 2003.

[37] Y. Yang, K.-S. Chen, L. Tsang, and L. Yu, "Depolarized backscattering of rough surface by AIEM model," *IEEE J. Sel. Topics Appl. Earth Observ. Remote Sens.*, vol. 10, no. 11, pp. 4740–4752, Nov. 2017.

[38] A. K. Fung *et al.*, "A modified IEM model for: Scattering from soil surfaces with application to soil moisture sensing," in *Proc. IEEE Int. Geosci. Remote Sens. Symp. (IGARSS)*, May 1996, vol. 2, no. 2, pp. 1297–1299.

[39] Y. Yang and K.-S. Chen, "Full-polarization bistatic scattering from an inhomogeneous rough surface," *IEEE Trans. Geosci. Remote Sens.*, vol. 57, no. 9, pp. 6434–6446, Sep. 2019.

[40] K. J. Pascoe, "Reflectivity and transmissivity through layered, lossy media: A user-friendly approach," Graduate School Eng. Manage., Air Force Inst. Technol., Wright-Patterson Air Force Base, OH, USA, Tech. Rep. AFIT/EN-TR-01-07, 2001.

[41] L. Tsang, J. A. Kong, and K.H. Ding, *Scattering of Electromagnetic Waves–Theories and Applications*, New York, NY, USA: Wiley, 2000.
[42] F. Ulaby and D. Long, *Microwave Radar and Radiometric Remote Sensing*. Ann Arbor, MI, USA: Univ. Michigan, 2014.
[43] Y. Yang and K. S. Chen, "Polarized backscattering from randomly anisotropic rough surface," *IEEE Trans. Geosci. Remote Sens*, vol. 57, no. 9, pp. 6608–6618, Sep. 2019.
[44] F. T. Ulaby and C. Elachi, *Radar Polarimetry for Geoscience Application*. Norwood, MA, USA: Artech House, 1990.

Ying Yang (Member, IEEE) received the B.S. degree in mathematics from China Three Gorges University, Yichang, China, in 2014, and the Ph.D. degree in cartography and geographic information systems from the Institute of Remote Sensing and Digital Earth (RADI), University of Chinese Academy of Science (UCAS), Beijing, China, in 2019.

She is a Post-Doctoral Research Associate with the Guilin University of Technology, Guilin, China. Her research interests include modeling and measurements of microwave scattering and analysis of remote sensing data with applications to terrain and sea.

Dr. Yang received the Young Scientist Award from the IEICE International Conference on Space, Aeronautical and Navigational Electronics (ICSANE), Jeju, South Korea, in 2019, and the 2019 Excellence Award by the President of the Chinese Academy of Sciences. She served as the Chair for the Beijing Chapter IEEE GRSS Student Branch (2016−2018) and has served as a Social Media Ambassador (SMA) for the IEEE GRSS since 2019.

Kun-Shan Chen (Fellow, IEEE) received the Ph.D. degree in electrical engineering from The University of Texas at Arlington, Arlington, TX, USA, in 1990.

From 1992 to 2014, he was a Professor with National Central University, Taoyuan City, Taiwan. From 2014 to 2019, he was with the Institute of Remote Sensing and Digital Earth, Chinese Academy of Sciences, Beijing, China. Since 2019, he has been a Professor with the Guilin University of Technology, Guilin, China, where his research interests include microwave remote sensing theory, modeling, system, and measurement, and intelligent signal processing and data analytics for radar. He has authored and co-authored over 160 referred journal articles and contributed 10 book chapters, is the Co-Author (with A. K. Fung) of the "*Microwave Scattering and Emission Models for Users*," Artech House, 2010, the Author of the "*Principles of Synthetic Aperture Radar: A System Simulation Approach*," CRC Press, 2015, and the Co-Editor (with X. Li, H. Guo, and X. Yang) of the "*Advances in SAR Remote Sensing of Ocean*," CRC Press, FL, USA, 2018, and the "*Radar Scattering and Imaging of Rough Surface: Modeling and Applications with MATLAB*," CRC Press, 2020.

Dr. Chen's academic activities include as a Guest Editor of the IEEE Transactions on Geoscience and Remote Sensing Special Issue on Remote Sensing for Major Disaster Prevention, Monitoring, and Assessment (2007), a Guest Editor for the Proceedings of IEEE Special Issue on Remote Sensing for Natural Disaster (2012), an Adcom Member of the IEEE GRSS (2010−2014), the Founding Chair of the GRSS Taipei Chapter, an Associate Editor of the IEEE TRANSACTIONS ON GEOSCIENCE AND REMOTE SENSING since 2000, and a Founding Deputy Editor-in-Chief of the IEEE JOURNAL OF SELECTED TOPICS IN APPLIED EARTH OBSERVATIONS, AND REMOTE SENSING (2008–2010). He serves as the guest editor for the special issue on Data Restoration and Denoising of Remote Sensing Data, and special issues on Radar Imaging Theory, Techniques, and Applications, both for Remote Sensing, and was the Co-Chair of the Technical Committee for IGARSS 2016 and IGARSS2017. He served as a member for the Editorial Board of the PROCEEDINGS OF THE IEEE(2014–2019), and has been a member of the Editorial Board of the IEEE ACCESS since 2020.

Xiaofeng Yang (Senior Member, IEEE) received the B.S. degree in environmental science from Sichuan University, Chengdu, China, in 2005, and the Ph.D. degree in cartography and geographic information systems from the Institute of Remote Sensing Applications (IRSA), Chinese Academy of Sciences (CAS), Beijing, China, in 2010.

During his Ph.D. program (2009–2010), he was a Visiting Research Scientist with the Department of Atmospheric and Oceanic Science, University of Maryland, College Park, MD, USA. From 2010 to 2012, he was an Assistant Professor with IRSA/CAS. From 2013 to 2015, he was an Associate Professor with the Institute of Remote Sensing and Digital Earth (RADI)/CAS, where he is a Full Professor with the State Key Laboratory of Remote Sensing Science. He has also participated in the development of various types of operational ocean products in China coastal waters from environmental satellite data. He has also served as a reviewer for several international academic journals. His research interests include satellite oceanography, synthetic aperture radar image processing, and marine atmospheric boundary layer process studies.

Zhao-Liang Li (Senior Member, IEEE) received the Ph.D. degree in remote sensing from the University of Strasbourg, Strasbourg, France, in 1990.

He joined the Institute of Agricultural Resources and Regional Planning, Beijing, China, in 2012. Since 1992, he has been a Research Scientist with CNRS, Illkirch-Graffenstaden, France. He has participated in many national and international projects. His main expertise fields are in thermal infrared radiometry, parameterization of land surface processes at large scale, as well as the assimilation of satellite data to land surface models.

Jiangyuan Zeng (Member, IEEE) received the B.S. degree from Wuhan University, Wuhan, China, in 2010, and the Ph.D. degree from the Institute of Remote Sensing and Digital Earth, Chinese Academy of Sciences, Beijing, China, in 2015.

He is an Associate Professor with the State Key Laboratory of Remote Sensing Science, Institute of Remote Sensing and Digital Earth, Chinese Academy of Sciences. His research interests include microwave remote sensing of geophysical parameters (particularly soil moisture), hydrological applications of satellite remote sensing, and bistatic scattering of soil surfaces.

Dr. Zeng received the "Li Xiaowen" Youth Award for Remote Sensing Science in 2019, the Young Scientist Award (including Cash Award) from the Progress in Electromagnetics Research Symposium (PIERS) in 2018, the Young Scientist Award from the International Union of Radio Science (URSI) in 2017, and the Excellent Doctoral Dissertation of the Chinese Academy of Sciences Award in 2016.